Experimental investigations of hard x-ray source produced by picosecond laser-irradiated solid target

Li, M.-T.; An, H.-H.; Hu, G.-Y.; Xiong, J.; Lei, A.-L.; Xie, Z.-Y.; Wang, C.; Wang, W.; Zhang, Z.-C.; Huang, L.;

Originally published:

January 2022

Physics of Plasmas 29(2022)1, 013107-1-013107-11

DOI: https://doi.org/10.1063/5.0064541

Experimental Investigations of Hard X-ray Source Produced by Picosecond Laser Irradiated Solid Target

Meng-ting Li[#1], Hong-hai An[#2], Guang-yue Hu*[1, 3], Jun Xiong[2], An-le Lei[2], Zhi-yong Xie[2], Chen Wang[2], Wei Wang[2], Zhen-chi Zhang[1], Lin-gen Huang[4]

[1]*CAS Key Laboratory of Geospace Environment & Department of Engineering and Applied Physics, University of Science and Technology of China, Hefei, Anhui 230026, China*

[2]*Shanghai Institute of Laser Plasma, CAEP, Shanghai 201899, China*

[3]*CAS Center for Excellence in Ultra-intense Laser Science(CEULS)，Shanghai 200031，China*

[4]*Helmholtz-Zentrum Dresden-Rossendorf (HZDR), Bautzner Landstraße 400, D-01328 Dresden, Germany*

[#]*Meng-ting Li and Hong-hai An contributes equally to this work*

**E-mail: gyhu@ustc.edu.cn*

ABSTRACT

Measurements of K_α line and bremsstrahlung continuous x-ray emission from high-intensity laser irradiated thin targets are presented. The experiments were performed at the SG-II UP Petawatt laser. Self-standing Sn foils varying thicknesses and Sn foils backed by the thick substrate were irradiated by the laser pulses up to 300 J of energy with peak intensity higher than 10^{18} W/cm^2. A transmission curved crystal spectrometer and a filter-stack spectrometer were used to measure the K_α line and bremsstrahlung x-rays spectral distribution respectively. Both K_α and 70-200 keV x-ray yields decrease 3-5 folds for target backed by the substrate. 2-4 folds reduction of K_α and 70-200 keV x-ray yields for the 8.5 μm targets relative to 50 μm targets was observed. Moreover, a significant background x-ray emission generated from the target holder reduces the ratio of signal to noise. Adopting a low-Z material holder can mitigate the x-ray background noises. This study is instructive to optimize target design for the high-intensity laser-driven K_α or continuous x-ray sources.

I. INTRODUCTION

The rapid development of ultra-intense short-pulse laser-driven x-ray source [1-13] enabled by the chirped pulse amplification (CPA) technique[14] makes it ideal for the x-ray backlight radiography of fast evolving phenomena in high energy density (HED) experiments. High energy, monoenergetic laser-produced K_α from several keV to tens of keV has been used as a backlighter source for measuring the density in shocked material to deduce the equation of state (EOS) at high-density and high-pressure conditions[15-17]. Continuum emission up to hundreds of keV is used for diagnosing the imploded capsule in inertial confined fusion (ICF)[18-22]. In these applications, a sufficient number of diagnostic photons is critical for making accurate measurement of the material density.

Previous works have shown the line-emission and broadband x-ray yields are heavily affected by the electron recirculation caused by the electrostatic fields surrounding the target surface [23-26]. A fraction of hot electrons escapes from the laser-irradiated target, leading to a sheath electrostatic field at both sides of the target. Some of the subsequent hot electrons are reflected by the sheath field at the rear side of the target, then travel back to the front surface and are re-accelerated by the laser fields[27]. A similar process also occurs at the front surface, which makes the electrons recirculate within the target until they escape from the sheath fields or exhaust their energy. This mechanism has been extensively explored in the context of x-ray emission, as well as hot electron transport[28-30], proton acceleration[31], ionization, and magnetic fields generation[32].

Many efforts have been devoted to study the effect of electron recirculation on K_α yields. It was shown that the recirculation effect enhances the K_α yields up to ten-folds in the relativistic laser intensity[23, 24, 26, 33, 34]. The number and temperature of continuum x-ray emissions at MeV and below can also be enhanced [25, 35-37]. Compant *et. al.* has shown that the recirculation mechanism increases the number of bremsstrahlung photons below 4 MeV by 2 times, but have nearly no effect above 10 MeV[25]. Continuum emission of 70-200 keV is particularly important for the x-ray radiography in HEDP experiments such as ICF. The energy conversion efficiency of 70-200 keV x-rays ($CE_{70\text{-}200}$) measured by LLNL group has shown a power scaling with the laser intensity below 10^{19} W/cm^2, typically be in the range of 10^{-4}-10^{-3}[18-22]. The experiments performed by Borm *et al.* [38] had a lower $CE_{70\text{-}200}$ which saturated at 10^{-4} in the wide-range intensities of 10^{17}-10^{21} W/cm^2. A simple semi-analytical model has predicted that the electron recirculation increases $CE_{70\text{-}200}$ by several to even one hundred folds depending on the laser intensity[39]. However, to the best of our knowledge, there is no reported experimental measurement showing of how much the mechanism affect the $CE_{70\text{-}200}$.

Assuming all the hot electrons are reflected between the front and rear surfaces of a foil target and interact with the material until their energy is exhausted in the target volume, the analytical models show that the K_α production will drop with increasing thickness if its absorption by the target material is taken into account[40, 41]. Moreover, the potential energy of the sheath field on the target surface is finite, and only the electrons with lower kinetic energy than this potential energy can be constrained. When target thickness decreasing, the sheath field is increased and can constrain more energetic electrons[42, 43]. So,

the thinner foil targets will produce more intense radiation. However, the electrons below the sheath potential energy does not necessarily deposit their energy completely inside the target. They may escape from the target before the energy is exhausted. Previous experiment suggested that the effective recirculation is limited for a few reasons including the plasma gradient at the front surface and electron beam divergence[36]. Through the PIC output of electron trajectories in Ref. [25], we can observe more intuitively that some electrons escape from the target before exhausting their energy after recirculating several times. Direct evidence of the electron escape during the recirculation can be observed from the K_α measurements of a double-layer target geometry as discussed in Part III. Understanding the electron escaping process will be beneficial for us to better control the laser-driven K_α or continuous x-ray resources in related applications.

This work reports the measurements of both K_α and continuum x-rays below 1 MeV produced by the picosecond laser driven high-Z Sn foil targets. First, a 1 mm-thick aluminum foil was adhered to the rear surface of the Sn target to suppress the electron recirculation, as shown in figure 1(c). It makes the x-ray yields drop by 3-5 folds for both K_α and continuum emissions. Second, the effect of the target thickness was explored by comparing the hard x-rays emitted from the self-standing 50 μm and 8.5 μm Sn foils under the similar laser conditions. We found a 2-4-folds reduction in x-ray yields from the thinner foils due to more escaping electrons. Finally, the holder (see figure 1(c)) material was varied in some shots. It was found that using a high-Z Fe holder will cause more intense background x-ray noises. So a low-Z holder is suggested to improve the performance of these sources for x-ray radiography applications.

II. EXPERIMENTAL SETUP

The experiments were performed using the SG-II UP petawatt picosecond laser[44] (central wavelength of 1053 nm) at Shanghai Institute of Optics and Fine Mechanism (SIOM). A sketch of the experimental setup is shown in figure 1(a). The laser pulse was focused by an f/2.5 off-axis parabolic mirror onto the target, with an incident angle of 21° relative to the target normal. The laser energy was 300 J or 150 J, with pulse duration of 1 ps. Sn or Cu foil targets hold by CH plastic frames (named "holder") were driven by laser pulses and produced hard x-ray sources. In some shots, double-layer targets that consisted of two foils separated by a certain distance were used (see figure 9). And the CH holders were replaced by Fe holders in few shots. The parameters of laser and target for each shot are given in Table I.

FIG. 1 (a) Sketch of the experimental setup. (b) A measured laser spot from the x-ray pinhole camera (#09), and the central axis lineouts in the X and Y dimensions. (c) Illustration of target structure, which shows a foil target with substrate and target holder. Note that not all shots have a substrate.

TABLE I. Laser and target parameters in the experiments.

Shot #	Energy (J)	Duration (ps)	Laser spot size (μm)	Intensity (W/cm^2)	Target

09	135.7	0.92	42×51	8.77×10^{18}	10μmCu
11	279.8	0.87	66×70	8.86×10^{18}	50μmSn
12	259.3	1.09	88×77	4.47×10^{18}	Double-layer (Fe holder)
14	274.0	0.98	63×55	1.03×10^{19}	Double-layer
15	137.8	0.54	73×73	6.10×10^{18}	15μmCu (Fe holder)
16	272.0	1.20	63×77	5.95×10^{18}	50μmSn+1mmAl (sub.)
17	293.6	1.41	60×78	5.66×10^{18}	50μmSn
18	311.9	1.41	51×83	6.65×10^{18}	8.5μmSn
19	300.2	1.14	92×98	3.72×10^{18}	Double-layer
20	294.9	0.92	66×78	7.93×10^{18}	8.5μmSn

*Double-layer: A double-layer target consists of a 15 μm Cu foil and a 50 μm Sn foil separated by a certain distance.

We fielded an improved x-ray pinhole camera (PHC)[45] to measure the x-ray spot sizes, a filter-stack spectrometer (FSS)[46, 47] and a transmission curved crystal spectrometer (TCS)[48, 49] to measure the hard x-ray spectra, and an electron magnetic spectrometer (EMS) to measure the escaping electron spectra. All the detectors were placed inside the target chamber on the equatorial plane.

The x-ray spots of 0.5-2.5 keV x-ray produced by laser irradiated targets were measured by the PHC, which consisted of pinhole, filters, and a grazing-incidence metal mirror. PHC was arranged at the front side with 15° view angle relative to the target normal. The x-ray spot sizes of this spectral range were considered as the laser focal spot sizes, and used to calculate the laser intensities. The full width at half maximum (FWHM) of the spot sizes were measured (64±13) μm in X dimension and (71±11) μm in Y dimension, leading the laser intensities to vary between 10^{18}-10^{19} W/cm^2. Figure 1(b) shows one of the measured spot images.

K_α and K_β line emissions from Sn with energies of 25.044 keV, 25.271 keV, 28.444 keV, and 28.486 keV were recorded using the TCS which was placed at the rear side of the target with a view angle of 30° relative to the target surface and 310 mm apart. The sensitivity of the IP was taken from calibration result from Ref. [50]. The diffraction efficiency of the curved crystal was obtained by numerically solving the Takagi–Taupin equations using the XOP codes[48]. The collimating aperture at the head of the TCS was used not only for alignment but also for obtaining images of x-ray sources (pinhole imaging), to investigate the influence of holder materials.

Bremsstrahlung hard x-ray emissions in the range from 50 keV to 1 MeV were measured with a 15 channels FSS which was placed at the front side of the target with a view angle of 30° relative to the target surface and 350 mm apart. A lead collimating tube and a pair of magnets with 0.4 T magnetic field over 15 cm length were incorporated to deflect the incident hot electrons with kinetic energy less than 20 MeV. Bremsstrahlung spectrum was reconstructed by Greval algorithm[51]. When calculating the radiation energy of K-line or continuum emission, the photons were assumed to emit isotropic over 4π solid angle.

III. EXPERIMENTAL RESULTS AND ANALYSIS

A. The effect of substrate on hard x-ray yields

In shot #16, an aluminum substrate of 1 mm-thickness was adhered to the planar Sn foil with the same lateral area. The electrons leaving the rear side is absorbed by the substrate thus suppressing recirculation. The target charging by the escaping electrons is compensated by the cold return currents from the substrate. Schematics of the self-standing Sn foil (#11/#17) and the substrate-backed Sn foil (#16) are shown in figure 2. Sn foils are 50 μm thick in both cases. Figure 3 presents the raw IP scan images recorded with the TCS, on which the line emissions of $K_{\alpha 1}$, $K_{\alpha 2}$, $K_{\beta 1}$ and $K_{\beta 2}$ are clearly visible. Figure 4 presents the characteristic K-line spectra. For the substrate-backed target, the x-rays are partially absorbed by the substrate before entering the detector. Thus, the spectrum corrected for absorption is also shown in green in the figure. In order to compare the intensities of line emissions more intuitively, we subtracted the uniform bremsstrahlung background from the original spectra (The original spectra are not shown in this paper), and then normalized the background-subtracted spectra according to the laser energies for each shot. The background intensities equal to the mean intensities of the continuum emissions in the vicinity of the K_α-line. Throughout the text, all the K-line spectra are background-subtracted and normalized according to the laser energies.

FIG. 2 Schematics of (a) self-standing Sn foil and (b) substrate-backed Sn foil.

FIG. 3 Raw IP scan images recorded with the TCS for (a) shot #11: self-standing 50 μm Sn foil, (b) shot #17: self-standing 50 μm Sn foil, and (c) shot #16: 50 μm Sn foil with substrate.

FIG. 4 Characteristic K-line spectra of self-standing 50 μm Sn foil (#11/#17) and 50 μm Sn foil with substrate (#16). The spectrum corrected for absorption by the substrate is also shown (labeled *#16 with sub. (corrected)*). Throughout the text, the spectra are bremsstrahlung background-subtracted and normalized according to the laser energies.

The discrepancy in line intensities between the two shots of self-standing target (#11/#17) may be caused by different laser intensities (8.86×10^{18} W/cm^2 vs 5.66×10^{18} W/cm^2). It is consistent with the results of previous experiments and semi-analytical models, which predicted that for a sufficiently thin foil, the energy conversion efficiencies of K_α increase slowly with the laser intensities of 10^{18}-10^{19} W/cm^2 [23, 52]. In this paper, the energy conversion efficiency from laser to the K_α, i.e. $CE(K_\alpha)$, were calculated by integrating the photon energies in the range of 25-25.4 keV from the spectra, and then multiplying by 4π to obtain the angle-integrated energies. $CE(K_\alpha)$ is 1.4×10^{-4} for the substrate scheme (#16) and $4.3/3.4\times10^{-4}$ for the self-standing foil (#11/#17). Thus, the substrate reduced the radiation energy of K_α to 1/4-1/3 of that without the substrate. This result is similar to the previous experiments using Cu foils

irradiated by the laser pulses of 10^{18} W/cm^2, which has shown $CE(K_\alpha)$ is 2×10^{-4} and 7×10^{-5} with and without substrate respectively[23].

Figure 5 shows the broadband bremsstrahlung spectra normalized by laser energies. To clearly present the influence of the substrate in the substrate-backed scheme, we calculated the bremsstrahlung contributed only by the 50 μm Sn foil as shown in blue dash line (labeled *#16 with sub. (only Sn)*). Our previous simulations[39] have predicted that in absence of electron recirculation, the intensity of bremsstrahlung hard x-rays is proportional to $Z\rho$L, where Z is the atomic number of the target material, ρ is the mass density, and L is the target thickness. Accordingly, the 50 μm Sn contributes one-third of the total radiation when electron recirculation is completely suppressed by the substrate. Here the absorption of x-rays by target material is neglected, which is plausible under the conditions of tens of keV hard x-rays penetrating through 1 mm-thick aluminum.

FIG. 5 Bremsstrahlung spectra of 50 μm Sn foil with substrate (#16) and self-standing 50 μm Sn foil (#11). The spectra labeled as "*only Sn*" is contributed only by the 50 μm Sn foil in the substrate-backed target (#16).

It can be observed that the substrate decreased the bremsstrahlung emissions of 50-600 keV, and the extent of this decrease decays with photon energy getting higher. By comparing the bremsstrahlung spectra from the self-standing Sn foil and that contributed only by the Sn foil in the substrate-backed target, it's found that the electron recirculation enhanced the x-ray photon number 4 times with energy below 1 MeV. We calculated the energy conversion efficiency from laser to the bremsstrahlung x-rays of 70-200 keV, i.e. $CE_{70\text{-}200}$, to be 5.3×10^{-4} for the substrate-backed target with electrons single-passing through the 50 μm Sn (*#16 with sub. (only Sn)*), and 2.3×10^{-3} for the self-standing target with the effect of electron recirculation (*#11 self-standing*). Therefore, in the application of radiography using a micro-wire target, such as Compton radiography for ICF, the substrate should be as thin as possible to avoid destroying the electron recirculation and thus leads to brighter x-ray source.

B. The effect of target thickness

Figure 6 compares the characteristic line emissions of self-standing Sn foils with different thicknesses. The experimental results of the 8.5 μm Sn (#18/#20) exhibit good reproducibility. The conversion efficiency of laser energy to the line emissions $CE(K_\alpha)$ is 3.4×10^{-4} for the 50 μm Sn (#17) and 1.6×10^{-4} /2.0×10^{-4} for the 8.5 μm Sn (#18/#20). Meanwhile, the thicker foil shows a more intense broadband radiation than the thinner foil, as seen in figure 7. There is a three-fold difference in the total number of photons in the range of 50 keV-1 MeV for the two thicknesses, and $CE_{70\text{-}200}$ is 2.3×10^{-3} for the 50 μm and 6.4×10^{-4} for the 8.5 μm.

FIG. 6 Characteristic K-line spectra of self-standing Sn foil with thickness of 8.5 μm and 50 μm.

FIG. 7 Bremsstrahlung spectra of self-standing Sn foil with thickness of 8.5 μm and 50 μm, and associated energy-dependent ratio of the two intensities.

The weaker K_α and bremsstrahlung yields from the thinner foils (8.5 μm) indicate that the thinner foil led more escaping hot electrons. Therefore, to maximize the hard x-ray sources using a thin foil as the radiation target, the optimized target thickness is to balance the competing effects of hot electron recirculation and escaping. Previous Monte Carlo simulations[53] showed that there is an optimum thickness of 20 μm for K_α source for Cu foil by including the sheath fields on the target surfaces.

The blue dash line in figure 7 shows the energy-dependent ratio of the bremsstrahlung intensities for the two thickness cases. It shows that the extent of the reduction is larger at higher photon energies, which is 2 folds at 50 keV, while up to 10 folds when above 500 keV. As a result, the thinner target presents a lower bremsstrahlung temperature than the thicker one. A reason of the radiation temperature decrease is related to the escaping electron, as measured by the EMS in the target normal direction. As seen in figure 8, the number of measured escaping electrons from the thinner foil is much higher above 1.5 MeV. The lower number below 1.5 MeV may be due to the fact that the electrons in the thinner foil are more divergent. It may be caused by more strong filaments forming and a lack of azimuthal field structure in the thinner foil, as discussed by the previous simulation works[30, 32]. However, the measure electron population in the thin target exceeds the thicker foil above 1.5 MeV. This means that the thinner foil had a larger proportion of high-energy escaping electrons to the total escaping electrons, resulting in a lower-temperature electrons interacting with target, and thus a lower radiation temperature.

FIG. 8 Spectra of the escaping electrons recorded using the EMS placed at the rear side of the target in the normal direction.

C. Measurement of second-layer emissions

Since a large amount of hot electrons escape from the foil before exhausting their energy, they could further excite x-rays by placing another foil behind the first foil. As shown in figure 9, a double-layer target was used in shot #19, which consists of a 15 μm-thick Cu foil and a 50 μm-thick Sn foil separated by 0.39 mm using two PC plastic blocks. The laser was irradiated onto the Cu target. Figure 9 compares the K-line emissions from the second layer of Sn foil with the single-layer Sn foil (self-standing or substrate-backed). The measured $CE(K_\alpha)$ of the second layer is 2.0×10^{-4}, which is half of the self-standing single layer (#11), but twice higher than the substate-backed single layer (#16).

FIG. 9 Characteristic K-line spectra of double-layer target (#19), self-standing Sn foil (#11), and substrate-backed Sn foil (#16). The Sn foils in the three kinds of structures are all 50 μm thick. Insert is the diagram of the double-layer Cu-Sn target of shot #19.

We can expect a scenario that the laser beam incident on the Cu foil generates a bunch of hot electrons which firstly recirculates around the Cu foil, excite x-rays, and loses part of their energy. Some electrons escape from the Cu foil and then hit the Sn layer behind. Despite less electrons than the initial generated ones interacting with the second layer, more intense x-rays are excited from the second layer than the case of electrons passing through the foil only once(#16). This may be due to the fact that these escaping electrons also recirculate in the second layer. Moreover, for this experimental condition, we would expect copious amount of TNSA-accelerated protons also contribute to the emissions of the second-layer. The ionization cross section for protons below 5 MeV is about 1/10 of that of escaping electrons. Since we did not measure the energy spectra of protons, a quantitative comparison of the contributions from protons and escaping electrons is difficult. Further work is needed to confirm this assumption.

D. The influence of holder material on imaging

Two couples of targets held with different materials (Fe and CH) were compared. One couple is single-layer Cu foils (#12). Another couple is double-layer targets consisting of a 15 μm Cu and a 50 μm Sn foils (#14), as depicted in figure 10(a) and (b). The Sn is half height of the Cu. In shot #12, the Cu foil is glued to a Fe holder and separated from the Sn by a 1.05 mm-thick CH block. In shot #14, the Cu and Sn are glued on the two sides of the CH holder, with a distance of 1.05 mm.

FIG. 10 Schematic diagrams of the double-layer Cu-Sn targets using (a) Fe or (b) CH holders. (c) Raw IP scan images recorded with the TCS for the double-layer Cu-Sn targets (#12/#14) and the single-layer Cu foils (#15/#09) held by different holders. (d) Bremsstrahlung spectra of Cu foils held by different holders.

Figure 10(c) shows the IP scan images recorded by the TCS for the four shots which exhibit distinct difference between the Fe and CH holders. For the double-layer Cu-Sn targets, the one with CH holder generated a more clear x-ray spectrum in which the continuous background is weak enough that the characteristic lines of $K_{\alpha 1}$, $K_{\alpha 2}$, $K_{\beta 1}$, and $K_{\beta 2}$ are clearly observed. In contrast, with a Fe holder, the lines are hidden in an intense continuous background, and the imaging of the x-ray source splits into three separated spots, which are induced by the Fe holder. The spots and intense background also appear for the single-layer Cu foil with Fe holder.

Figure 10(d) shows the bremsstrahlung spectra of the two shots of single-layer Cu foils. The number of radiated photons of shot #15 with Fe holder was four times that of shot #09 with CH holder. The difference in target thickness will not cause such a big difference in radiation intensity. Combined with the IP images above, we can conclude that the stronger emissions of shot #15 were mainly induced by the Fe target holder.

This is most likely due to the hot electrons having a large range even in the solid density target, thus spreading out laterally to reach and interact with the holder. At the very beginning, hot electrons are accelerated to the different directions by different absorption mechanisms. When Brunel-type resonance

absorption[54] is dominant, the electrons are mainly directed near the target normal direction. When the pondermotive force becomes the main mechanism, the hot electrons are generated in the direction of laser beam propagation[55]. With a large plasma scale length, the accelerated electrons will obtain a large transverse velocity[56-59]. This may be attributed to the instabilities such as filamentation and self-focusing of the laser beam in the under-dense plasma[60], or the electrons scattered by quasistatic magnetic fields formed by the Weibel instability[61], or the curvature of the relativistic critical surface in a longer plasma scale length[58]. In the picosecond laser interaction with a solid target, these processes are time dependent and triggered simultaneously[56, 62-65]. Typically, the divergence angles of accelerated electrons are up to 50°[66-68]. The recirculation movement will further increase the lateral displacement of the electrons beam, by spoiling the formation of self-generated magnetic field which can collimate the electron beam[30, 32] and making the electrons to drift laterally and randomly as many experimental studies have revealed[25, 69, 70]. In addition, an electron beam emitting along the surface of the target is formed due to the confinement of the surface quasistatic electromagnetic fields when the plasma density scale length is small[71]. Experimental study by Buffechoux *et al.* [29] has shown that the electrons at the target surface will move ~10s of μm extent to reach the target edges and be reflected to form a transverse recirculation. With the large lateral displacement, the electrons can easily reach the target holder material even when the surface side length is on the scale of millimeters as in our experiment. Especially, in those micro-volume target for point projecting radiography, a large amount of hot electrons do not deposit their energy completely in the backlighter target, but hit the holder and generate x-ray noises. Therefore, the holders for backlighter targets in point projecting radiography experiments should be low-Z materials such as CH in order to restrain x-ray noises.

IV. DISCUSSION AND CONCLUSIONS

Figure 11 and figure 12 summarize the conversion efficiency $CE(K_\alpha)$ and $CE_{70\text{-}200}$ respectively in our experiments marked with the blue symbols, where different markers represent different target thicknesses or geometries (seen in the figures). The results of $CE(K_\alpha)$ and $CE_{70\text{-}200}$ from previous picoseconds laser experiments are also presented. Figure 12 shows the results of a 1D electron transport calculation coupled with bremsstrahlung generation. It assumes a bunch of incident electrons following Boltzmann distribution, i.e. $f(E)\sim\exp(-E/T_e)$, recirculate between the front and rear surfaces of a 50 μm Sn foil. Different colors represent different maximum transmission distances as annotated in the figure. For example, when the maximum transmission distance equals to 300 μm ("*<300 μm*"), electrons will travel back and forth in the bulk target for a distance of 300 μm and then escape, or be absorbed by the material in case of shorter electron stopping range. The top line assumes all the electrons can circulate until their energy are completely lost in the foil ("*Complete*"). The bottom line assumes the electrons pass through the 50 μm-thick Sn foil only once without recirculation ("*<50 μm*"). Here, we employed Beg's scaling law to determine the electron temperature T_e, and the laser-to-electron energy conversion η was set to 0.4

referenced to the results from Ping *et al.* [60] at a similar laser intensity. The detailed process has been demonstrated in our previous work[39].

FIG. 11 Energy conversion efficiency from laser to the K_α emissions $CE(K_\alpha)$. The calculated $CE(K_\alpha)$ in our experiments are displayed in blue symbols. The red dot marks previous experimental result from Park *et al.*[72] using a 25 μm-thick Sn foil.

FIG. 12 Energy conversion efficiency from laser to the bremsstrahlung x-rays of 70-200 keV $CE_{70\text{-}200}$. Our experimental results (blue symbols), previous experimental results from Chen *et al.*[21] using 10 μm-thick Au foils (red dots) and Borm *et a*l. [38] using 5 μm-thick Au foils (blue squares) are presented. A semi-analytical model are displayed in solid lines, with different colors representing different maximum transmission distances.

In our experiments, the laser intensity is in the range of 5×10^{18}-10^{19} W/cm^2, which results in $CE(K_\alpha)$ in the range of 10^{-4}-5×10^{-4}. That's slightly higher than the results of Park *et al.*[72] at non-relativistic laser intensities. We note that since we have not experimentally calibrated the detection efficiency of TCS, the uncertainty of the quantitative results has not been calculated. Comparison with other published data should be treated carefully. But in the same round of experiments, it is helpful to compare the relative values at similar experimental conditions. The $CE(K_\alpha)$ of self-standing 50 μm Sn foils (#11/#17) is twice that of 8.5 μm Sn foils (#18/#20) and the second layer (#19), attributed to more effective reflected electrons interacting with the bulk target. The 50 μm Sn with a thick substrate (#16) has the lowest $CE(K_\alpha)\sim1.16\times10^{-4}$ since electrons just pass through the target once.

$CE_{70\text{-}200}$ in our experiments is in the range of 5×10^{-4}-3×10^{-3} with the laser intensities around 10^{19} W/cm^2. When approaching 10^{17} W/cm^2, the "*Complete*" curve is very close to the "*<300 μm*" curve, indicating that the electron energies are too low that most of the electrons can only transverse less than 300 μm distance, i.e. recirculate less than 3 times in the 50 μm-thick Sn foils. As the laser intensity increases, the recirculation of higher-energy electrons contributes significantly to the radiation. Moreover, in the case of the substrate-backed 50 μm Sn, a considerable number of electrons have the stopping range longer than 1 mm in the aluminum, especially those with initial energies higher than 1 MeV. These electrons may also recirculate in the substrate-backed target, making the measured *CE* fall between the "*<50 μm*" and "*<100 μm*" curves. We can expect that if a thicker Al substrate had been used, the *CE* would be reduced to be closer to the prediction of single-pass model ("*<50 μm*"). The *CE* of self-standing 50 μm foil is located at the "*<500 μm*" curve. We calculated the mean round number of the electrons to be 2.7 in this case. The *CE* of self-standing 8.5 μm foils are located at the "*<100 μm*" curve, leading a higher average round number, calculated to be 5. In this process, there are many uncertain factors causing the loss of electrons. For example, the electron may reach outside the lateral area where the sheath fields can confine it, or be accelerated to an opposite direction by the reflected lasers. So the integral cross-section for the electron group interacting with the material is reduced. Another reason for the loss of electrons in the thinner target

may be caused by the pre-plasma on the back surface formed by the pre-pulse generated shock waves. It will mitigate the electron reflection at the target rear. Experiments by Park *et al.*[4, 33] have shown that K_α production is independent of the foil thickness down to 2 μm for Cu and 12.5 μm for Ag, and a significant decrease has been observed below 2 μm for Cu foils. Researchers attributed the decrease observed below the critical thickness to an increased volumetric heating leading to a depletion of cold material, and to an increased transfer of hot electron energy into TNSA-accelerated protons. However, in our experiments, the maximum energy of protons measured for the two thicknesses is nearly the same. Volumetric heating should have little effect since the target surface areas (~mm^2) were much larger than those in their experiments (~10^4 μm^2). Understanding the electron escape for the thinner foil and the critical thickness of x-rays yield reduction is complicated and a worthy topic for our next work.

In conclusion, we explored the hard x-ray emitted by picoseconds laser-irradiated Sn foils in experiments. We found that the substrate suppresses the electron recirculation and decreases the line and continuum emissions. $CE(K_\alpha)$ and $CE_{70\text{-}200}$ are increased by a factor of 3.2 and 4.4 respectively without a substrate. The intensities of bremsstrahlung below 1 MeV are increased by 2-4 times depending on the photon energy. Therefore, the substrate used in a backlighter has to be as thin as possible in experiments. A moderate thickness is preferred to obtain the brightest x-ray sources, which is to optimize the effects of hot electron escape and electron recirculation. In our experiment for Sn foil targets, 50 μm was closer to this optimum thickness than 8.5 μm, with $CE(K_\alpha)$ and $CE_{70\text{-}200}$ 2.7 and 3.6 times that of the latter. If another foil is added behind the first thin foil to gather the escaping electrons, the x-ray production could possibly be further enhanced. This multi-layer target scheme might be an effective approach to utilize the escaping hot electrons and enhance the hard x-ray yields. This is a worthy topic for our next work. Finally, we also found that the interaction of the escaping electrons with target holder generates intense x-ray background noises. So it is benefit to use a low-Z material for the holder to reduce the background noises. This effect may be more pronounced in a micro-wire target for point projecting radiography than the foil targets as discussed in this paper.

ACKNOWLEDGEMENT

We acknowledge the SG-IIU technical staff at Shanghai Institute of Optics and Fine Mechanics for their support during the experiments. This work was supported by the Strategic Priority Research Program of Chinese Academy of Sciences (Grant No.XDB16000000), the National Natural Science Foundation of China (Grant Nos. 11775223, 11375197, 11605200, and 11275202), the Science Challenge Project (Grant No. TZ2016005), and the Open Fund of the State Key Laboratory of High Field Laser Physics (SIOM).

DATA AVAILABILITY STATEMENT

The data that supports the findings of this study are available within the article.

REFERENCE

1. Beg, F.N., A.R. Bell, A.E. Dangor, C.N. Danson, A.P. Fews, M.E. Glinsky, B.A. Hammel, P. Lee, P.A. Norreys, and M. Tatarakis, Physics of Plasmas **4** (2), 447-457 (1997).
2. Chen, L.M., P. Forget, S. Fourmaux, J.C. Kieffer, A. Krol, C.C. Chamberlain, B.X. Hou, J. Nees, and G. Mourou, Physics of Plasmas **11** (9), 4439-4445 (2004).
3. Glinec, Y., J. Faure, L.L. Dain, S. Darbon, T. Hosokai, J.J. Santos, E. Lefebvre, J.P. Rousseau, F. Burgy, B. Mercier, and V. Malka, Phys Rev Lett **94** (2), 025003 (2005).
4. Park, H.S., D.M. Chambers, H.K. Chung, R.J. Clarke, R. Eagleton, E. Giraldez, T. Goldsack, R. Heathcote, N. Izumi, M.H. Key, J.A. King, J.A. Koch, O.L. Landen, A. Nikroo, P.K. Patel, D.F. Price, B.A. Remington, H.F. Robey, R.A. Snavely, D.A. Steinman, R.B. Stephens, C. Stoeckl, M. Storm, M. Tabak, W. Theobald, R.P.J. Town, J.E. Wickersham, and B.B. Zhang, Physics of Plasmas **13** (5), 056309 (2006).
5. Courtois, C., R. Edwards, A. Compant La Fontaine, C. Aedy, M. Barbotin, S. Bazzoli, L. Biddle, D. Brebion, J.L. Bourgade, D. Drew, M. Fox, M. Gardner, J. Gazave, J.M. Lagrange, O. Landoas, L. Le Dain, E. Lefebvre, D. Mastrosimone, N. Pichoff, G. Pien, M. Ramsay, A. Simons, N. Sircombe, C. Stoeckl, and K. Thorp, Physics of Plasmas **18** (2), 023101 (2011).
6. Maddox, B.R., H.S. Park, B.A. Remington, C. Chen, S. Chen, S.T. Prisbrey, A. Comley, C.A. Back, C. Szabo, J.F. Seely, U. Feldman, L.T. Hudson, S. Seltzer, M.J. Haugh, and Z. Ali, Physics of Plasmas **18** (5), 056709 (2011).
7. Sefkow, A.B., G.R. Bennett, M. Geissel, M. Schollmeier, B.C. Franke, and B.W. Atherton, Phys Rev Lett **106** (23), 235002 (2011).
8. Compant La Fontaine, A., C. Courtois, and E. Lefebvre, Physics of Plasmas **19** (2), 023104 (2012).
9. Courtois, C., R. Edwards, A. Compant La Fontaine, C. Aedy, S. Bazzoli, J.L. Bourgade, J. Gazave, J.M. Lagrange, O. Landoas, L.L. Dain, D. Mastrosimone, N. Pichoff, G. Pien, and C. Stoeckl, Physics of Plasmas **20** (8), 083114 (2013).
10. Vaughan, K., A.S. Moore, V. Smalyuk, K. Wallace, D. Gate, S.G. Glendinning, S. McAlpin, H.S. Park, C. Sorce, and R.M. Stevenson, High Energy Density Physics **9** (3), 635-641 (2013).
11. Jarrott, L.C., A.J. Kemp, L. Divol, D. Mariscal, B. Westover, C. McGuffey, F.N. Beg, M. Suggit, C. Chen, D. Hey, B. Maddox, J. Hawreliak, H.S. Park, B. Remington, M.S. Wei, and A. MacPhee, Physics of Plasmas **21** (3), 031211 (2014).
12. Brambrink, E., S. Baton, M. Koenig, R. Yurchak, N. Bidaut, B. Albertazzi, J.E. Cross, G. Gregori, A. Rigby, E. Falize, A. Pelka, F. Kroll, S. Pikuz, Y. Sakawa, N. Ozaki, C. Kuranz, M. Manuel, C. Li, P. Tzeferacos, and D. Lamb, High Power Laser Science and Engineering **4**, 30 (2016).
13. Sawada, H., S. Lee, T. Shiroto, H. Nagatomo, Y. Arikawa, H. Nishimura, T. Ueda, K. Shigemori, A. Sunahara, N. Ohnishi, F.N. Beg, W. Theobald, F. Pérez, P.K. Patel, and S. Fujioka, Applied Physics Letters **108** (25), 254101 (2016).
14. Strickland, D. and G. Mourou, Optics Communications **55** (6), 447-449 (1985).
15. Benuzzi-Mounaix, A., M. Koenig, A. Ravasio, T. Vinci, N. Ozaki, M.R.l. Gloahec, B. Loupias, G. Huser, E. Henry, S. Bouquet, C. Michaut, D. Hicks, A. MacKinnon, P. Patel, H.S. Park, S.L. Pape,

T. Boehly, M. Borghesi, C. Cecchetti, M. Notley, R. Clark, S. Bandyopadhyay, S. Atzeni, A. Schiavi, Y. Aglitskiy, A. Faenov, T. Pikuz, D. Batani, R. Dezulian, and K. Tanaka, Plasma Physics and Controlled Fusion **48** (12B), B347 (2006).

16. Brambrink, E., H.G. Wei, B. Barbrel, P. Audebert, A. Benuzzi-Mounaix, T. Boehly, T. Endo, C.D. Gregory, T. Kimura, R. Kodama, N. Ozaki, H.S. Park, and M. Koenig, Phys Rev E Stat Nonlin Soft Matter Phys **80** (5 Pt 2), 056407 (2009).
17. Morace, A., L. Fedeli, D. Batani, S. Baton, F.N. Beg, S. Hulin, L.C. Jarrott, A. Margarit, M. Nakai, M. Nakatsutsumi, P. Nicolai, N. Piovella, M.S. Wei, X. Vaisseau, L. Volpe, and J.J. Santos, Physics of Plasmas **21** (10), 102712 (2014).
18. Tommasini, R., H.-S. Park, P. Patel, B. Maddox, S. Le Pape, S.P. Hatchett, B.A. Remington, M.H. Key, N. Izumi, M. Tabak, J.A. Koch, O.L. Landen, D. Hey, A. MacKinnon, J. Seely, G. Holland, L. Hudson, and C. Szabo, *Development of Compton radiography using high-Z backlighters produced by ultra-intense lasers*, in *AIP Conference Proceedings*. 2007. p. 248-258.
19. Tommasini, R., A. MacPhee, D. Hey, T. Ma, C. Chen, N. Izumi, W. Unites, A. MacKinnon, S.P. Hatchett, B.A. Remington, H.S. Park, P. Springer, J.A. Koch, O.L. Landen, J. Seely, G. Holland, and L. Hudson, Rev Sci Instrum **79** (10), 10E901 (2008).
20. Tommasini, R., S.P. Hatchett, D.S. Hey, C. Iglesias, N. Izumi, J.A. Koch, O.L. Landen, A.J. MacKinnon, C. Sorce, J.A. Delettrez, V.Y. Glebov, T.C. Sangster, and C. Stoeckl, Physics of Plasmas **18** (5), 056309 (2011).
21. Chen, H., M.R. Hermann, D.H. Kalantar, D.A. Martinez, P. Di Nicola, R. Tommasini, O.L. Landen, D. Alessi, M. Bowers, D. Browning, G. Brunton, T. Budge, J. Crane, J.M. Di Nicola, T. Döppner, S. Dixit, G. Erbert, B. Fishler, J. Halpin, M. Hamamoto, J. Heebner, V.J. Hernandez, M. Hohenberger, D. Homoelle, J. Honig, W. Hsing, N. Izumi, S. Khan, K. LaFortune, J. Lawson, S.R. Nagel, R.A. Negres, L. Novikova, C. Orth, L. Pelz, M. Prantil, M. Rushford, M. Shaw, M. Sherlock, R. Sigurdsson, P. Wegner, C. Widmayer, G.J. Williams, W. Williams, P. Whitman, and S. Yang, Physics of Plasmas **24** (3), 033112 (2017).
22. Tommasini, R., C. Bailey, D.K. Bradley, M. Bowers, H. Chen, J.M. Di Nicola, P. Di Nicola, G. Gururangan, G.N. Hall, C.M. Hardy, D. Hargrove, M. Hermann, M. Hohenberger, J.P. Holder, W. Hsing, N. Izumi, D. Kalantar, S. Khan, J. Kroll, O.L. Landen, J. Lawson, D. Martinez, N. Masters, J.R. Nafziger, S.R. Nagel, A. Nikroo, J. Okui, D. Palmer, R. Sigurdsson, S. Vonhof, R.J. Wallace, and T. Zobrist, Physics of Plasmas **24** (5), 053104 (2017).
23. Neumayer, P., B. Aurand, M. Basko, B. Ecker, P. Gibbon, D.C. Hochhaus, A. Karmakar, E. Kazakov, T. Kühl, C. Labaune, O. Rosmej, A. Tauschwitz, B. Zielbauer, and D. Zimmer, Physics of Plasmas **17** (10), 103103 (2010).
24. Quinn, M.N., X.H. Yuan, X.X. Lin, D.C. Carroll, O. Tresca, R.J. Gray, M. Coury, C. Li, Y.T. Li, C.M. Brenner, A.P.L. Robinson, D. Neely, B. Zielbauer, B. Aurand, J. Fils, T. Kuehl, and P. McKenna, Plasma Physics and Controlled Fusion **53** (2), 025007 (2011).
25. Compant La Fontaine, A., C. Courtois, E. Lefebvre, J.L. Bourgade, O. Landoas, K. Thorp, and C. Stoeckl, Physics of Plasmas **20** (12), 123111 (2013).

26. Sawada, H., M.S. Wei, S. Chawla, A. Morace, K. Akli, T. Yabuuchi, N. Nakanii, M.H. Key, P.K. Patel, A.J. Mackinnon, H.S. McLean, R.B. Stephens, and F.N. Beg, Phys Rev E Stat Nonlin Soft Matter Phys **89** (3), 033105 (2014).
27. Gray, R.J., R. Wilson, M. King, S.D.R. Williamson, R.J. Dance, C. Armstrong, C. Brabetz, F. Wagner, B. Zielbauer, and V. Bagnoud, New Journal of Physics **20** (3), 033021 (2018).
28. Chen, H.U.I. and S.C. Wilks, Laser and Particle Beams **23** (04), 411-416 (2005).
29. Buffechoux, S., J. Psikal, M. Nakatsutsumi, L. Romagnani, A. Andreev, K. Zeil, M. Amin, P. Antici, T. Burris-Mog, A. Compant-La-Fontaine, E. d'Humieres, S. Fourmaux, S. Gaillard, F. Gobet, F. Hannachi, S. Kraft, A. Mancic, C. Plaisir, G. Sarri, M. Tarisien, T. Toncian, U. Schramm, M. Tampo, P. Audebert, O. Willi, T.E. Cowan, H. Pepin, V. Tikhonchuk, M. Borghesi, and J. Fuchs, Phys Rev Lett **105** (1), 015005 (2010).
30. Yuan, X.H., A.P.L. Robinson, M.N. Quinn, D.C. Carroll, M. Borghesi, R.J. Clarke, R.G. Evans, J. Fuchs, P. Gallegos, L. Lancia, D. Neely, K. Quinn, L. Romagnani, G. Sarri, P.A. Wilson, and P. McKenna, New Journal of Physics **12** (6), 063018 (2010).
31. Mackinnon, A.J., Y. Sentoku, P.K. Patel, D.W. Price, S. Hatchett, M.H. Key, C. Andersen, R. Snavely, and R.R. Freeman, Phys Rev Lett **88** (21), 215006 (2002).
32. Huang, L.G., H.P. Schlenvoigt, H. Takabe, and T.E. Cowan, Physics of Plasmas **24** (10), 103115 (2017).
33. Theobald, W., K. Akli, R. Clarke, J.A. Delettrez, R.R. Freeman, S. Glenzer, J. Green, G. Gregori, R. Heathcote, N. Izumi, J.A. King, J.A. Koch, J. Kuba, K. Lancaster, A.J. MacKinnon, M. Key, C. Mileham, J. Myatt, D. Neely, P.A. Norreys, H.S. Park, J. Pasley, P. Patel, S.P. Regan, H. Sawada, R. Shepherd, R. Snavely, R.B. Stephens, C. Stoeckl, M. Storm, B. Zhang, and T.C. Sangster, Physics of Plasmas **13** (4), 043102 (2006).
34. Myatt, J., W. Theobald, J.A. Delettrez, C. Stoeckl, M. Storm, T.C. Sangster, A.V. Maximov, and R.W. Short, Physics of Plasmas **14** (5), 056301 (2007).
35. Westover, B., A. MacPhee, C. Chen, D. Hey, T. Ma, B. Maddox, H.S. Park, B. Remington, and F.N. Beg, Physics of Plasmas **17** (8), 082703 (2010).
36. Makita, M., G. Nersisyan, K. McKeever, T. Dzelzainis, S. White, B. Kettle, B. Dromey, D. Doria, M. Zepf, C.L.S. Lewis, A.P.L. Robinson, S.B. Hansen, and D. Riley, Physics of Plasmas **21** (2), 023113 (2014).
37. McKeever, K., M. Makita, G. Nersisyan, T. Dzelzainis, S. White, B. Kettle, B. Dromey, M. Zepf, G. Sarri, D. Doria, H. Ahmed, C.L.S. Lewis, D. Riley, and A.P.L. Robinson, Physical Review E **91** (3), 033107 (2015).
38. Borm, B., D. Khaghani, and P. Neumayer, Physics of Plasmas **26** (2), 023109 (2019).
39. Li, M., G.-y. Hu, L. Huang, and J. Zheng, Plasma Physics and Controlled Fusion **62**, 095006 (2020).
40. Kostenko, O.F. and N.E. Andreev, Quantum Electronics **43** (3), 237-241 (2013).
41. Kostenko, O.F., Quantum Electronics **49** (3), 216-219 (2019).
42. Sentoku, Y., T.E. Cowan, A. Kemp, and H. Ruhl, Physics of Plasmas **10** (5), 2009-2015 (2003).
43. Ceccotti, T., A. Levy, H. Popescu, F. Reau, P. D'Oliveira, P. Monot, J.P. Geindre, E. Lefebvre, and P. Martin, Phys Rev Lett **99** (18), 185002 (2007).

44. Zhu, J., J. Zhu, X. Li, B. Zhu, W. Ma, X. Lu, W. Fan, Z. Liu, S. Zhou, and G. Xu, High Power Laser Science & Engineering **6**, e55 (2018).
45. Wang, C., H.H. An, J. Xiong, Z.H. Fang, Y.W. Wang, Z. Zhang, N. Hua, J.R. Sun, and W. Wang, Review of Scientific Instruments **88** (11), 113501 (2017).
46. Chen, C.D., J.A. King, M.H. Key, K.U. Akli, F.N. Beg, H. Chen, R.R. Freeman, A. Link, A.J. Mackinnon, A.G. MacPhee, P.K. Patel, M. Porkolab, R.B. Stephens, and L.D. Van Woerkom, Rev Sci Instrum **79** (10), 10E305 (2008).
47. Ming-hai, Y., T. Fang, Y. Yong-hong, C. Jia, Z. Tian-kui, H. Dan, W. Yu-chi, D. Ke-gong, Z. Bin, Y. Jing, W. Shao-yi, and G. Yu-qiu, Atomic Energy Science and Technology **51** (6), 1090-1095 (2017).
48. Sanchez del Rio, M., C. Ferrero, and V. Mocella, Proceedings of SPIE - The International Society for Optical Engineering **3151** (1), 312-323 (1997).
49. Yu, M.-h., G.-y. Hu, N. An, F. Qian, Y.-c. Wu, X.-d. Zhang, Y.-q. Gu, Q.-p. Wang, and J. Zheng, High Power Laser Science and Engineering **4**, 2 (2016).
50. Maddox, B.R., H.S. Park, B.A. Remington, N. Izumi, S. Chen, C. Chen, G. Kimminau, Z. Ali, M.J. Haugh, and Q. Ma, Rev Sci Instrum **82** (2), 023111 (2011).
51. Vourvopoulos, G. and M. Matzke, Proc SPIE **2867**, 598 (1997).
52. Nilson, P.M., W. Theobald, J. Myatt, C. Stoeckl, M. Storm, O.V. Gotchev, J.D. Zuegel, R. Betti, D.D. Meyerhofer, and T.C. Sangster, Physics of Plasmas **15** (5), 056308 (2008).
53. Zhao, J.C., L.H. Cao, Z.Q. Zhao, Z.J. Liu, C.Y. Zheng, H. Zhang, Y.Q. Gu, and J. Liu, Physics of Plasmas **25** (3), 033104 (2018).
54. Brunel, F., Phys Rev Lett **59** (1), 52-55 (1987).
55. Malka, G. and J.L. Miquel, Phys Rev Lett **77** (1), 75-78 (1996).
56. Santala, M.I., M. Zepf, I.I. Watts, F.N. Beg, E. Clark, M. Tatarakis, K. Krushelnick, A.E. Dangor, T. McCanny, I.I. Spencer, R.P. Singhal, K.W. Ledingham, S.C. Wilks, A.C. Machacek, J.S. Wark, R. Allott, R.J. Clarke, and P.A. Norreys, Phys Rev Lett **84** (7), 1459-62 (2000).
57. Ovchinnikov, V.M., D.W. Schumacher, M. McMahon, E.A. Chowdhury, C.D. Chen, A. Morace, and R.R. Freeman, Phys Rev Lett **110** (6), 065007 (2013).
58. Debayle, A., J.J. Honrubia, E. d'Humieres, and V.T. Tikhonchuk, Phys Rev E Stat Nonlin Soft Matter Phys **82** (3 Pt 2), 036405 (2010).
59. Courtois, C., A. Compant La Fontaine, O. Landoas, G. Lidove, V. Méot, P. Morel, R. Nuter, E. Lefebvre, A. Boscheron, J. Grenier, M.M. Aléonard, M. Gerbaux, F. Gobet, F. Hannachi, G. Malka, J.N. Scheurer, and M. Tarisien, Physics of Plasmas **16** (1), 013105 (2009).
60. Ping, Y., R. Shepherd, B.F. Lasinski, M. Tabak, H. Chen, H.K. Chung, K.B. Fournier, S.B. Hansen, A. Kemp, D.A. Liedahl, K. Widmann, S.C. Wilks, W. Rozmus, and M. Sherlock, Physical Review Letters **100** (8), 085004 (2008).
61. Adam, J.C., A. Heron, and G. Laval, Phys Rev Lett **97** (20), 205006 (2006).
62. Norreys, P.A., M. Santala, E. Clark, M. Zepf, I. Watts, F.N. Beg, K. Krushelnick, M. Tatarakis, A.E. Dangor, X. Fang, P. Graham, T. McCanny, R.P. Singhal, K.W.D. Ledingham, A. Creswell,

D.C.W. Sanderson, J. Magill, A. Machacek, J.S. Wark, R. Allott, B. Kennedy, and D. Neely, Physics of Plasmas **6** (5), 2150-2156 (1999).

63. Kemp, A.J. and L. Divol, Phys Rev Lett **109** (19), 195005 (2012).
64. Peebles, J., M.S. Wei, A.V. Arefiev, C. McGuffey, R.B. Stephens, W. Theobald, D. Haberberger, L.C. Jarrott, A. Link, H. Chen, H.S. McLean, A. Sorokovikova, S. Krasheninnikov, and F.N. Beg, New Journal of Physics **19** (2), 023008 (2017).
65. Iwata, N., S. Kojima, Y. Sentoku, M. Hata, and K. Mima, Nat Commun **9** (1), 623 (2018).
66. Sheng, Z.-M., Y. Sentoku, K. Mima, J. Zhang, W. Yu, and J. Meyer-ter-Vehn, Physical review letters **85** (25), 5340 (2000).
67. Stephens, R.B., R.A. Snavely, Y. Aglitskiy, F. Amiranoff, C. Andersen, D. Batani, S.D. Baton, T. Cowan, R.R. Freeman, T. Hall, S.P. Hatchett, J.M. Hill, M.H. Key, J.A. King, J.A. Koch, M. Koenig, A.J. MacKinnon, K.L. Lancaster, E. Martinolli, P. Norreys, E. Perelli-Cippo, M. Rabec Le Gloahec, C. Rousseaux, J.J. Santos, and F. Scianitti, Phys Rev E Stat Nonlin Soft Matter Phys **69** (6 Pt 2), 066414 (2004).
68. Green, J.S., V.M. Ovchinnikov, R.G. Evans, K.U. Akli, H. Azechi, F.N. Beg, C. Bellei, R.R. Freeman, H. Habara, R. Heathcote, M.H. Key, J.A. King, K.L. Lancaster, N.C. Lopes, T. Ma, A.J. MacKinnon, K. Markey, A. McPhee, Z. Najmudin, P. Nilson, R. Onofrei, R. Stephens, K. Takeda, K.A. Tanaka, W. Theobald, T. Tanimoto, J. Waugh, L. Van Woerkom, N.C. Woolsey, M. Zepf, J.R. Davies, and P.A. Norreys, Physical Review Letters **100** (1), 015003 (2008).
69. Nagel, S.R., H. Chen, J. Park, M. Foord, A.U. Hazi, T.J. Hilsabeck, S.M. Kerr, E.V. Marley, and G.J. Williams, Applied Physics Letters **110** (14), 144102 (2017).
70. Armstrong, C.D., C.M. Brenner, E. Zemaityte, G.G. Scott, D.R. Rusby, G. Liao, H. Liu, Y. Li, Z. Zhang, Y. Zhang, B. Zhu, P. Bradford, N.C. Woolsey, P. Oliveira, C. Spindloe, W. Wang, P. McKenna, and D. Neely, Plasma Physics and Controlled Fusion **61** (3), 034001 (2019).
71. Li, Y.T., X.H. Yuan, M.H. Xu, Z.Y. Zheng, Z.M. Sheng, M. Chen, Y.Y. Ma, W.X. Liang, Q.Z. Yu, Y. Zhang, F. Liu, Z.H. Wang, Z.Y. Wei, W. Zhao, Z. Jin, and J. Zhang, Physical Review Letters **96** (16), 165003 (2006).
72. Park, H.S., B.R. Maddox, E. Giraldez, S.P. Hatchett, L.T. Hudson, N. Izumi, M.H. Key, S. Le Pape, A.J. MacKinnon, A.G. MacPhee, P.K. Patel, T.W. Phillips, B.A. Remington, J.F. Seely, R. Tommasini, R. Town, J. Workman, and E. Brambrink, Physics of Plasmas **15** (7), 072705 (2008).

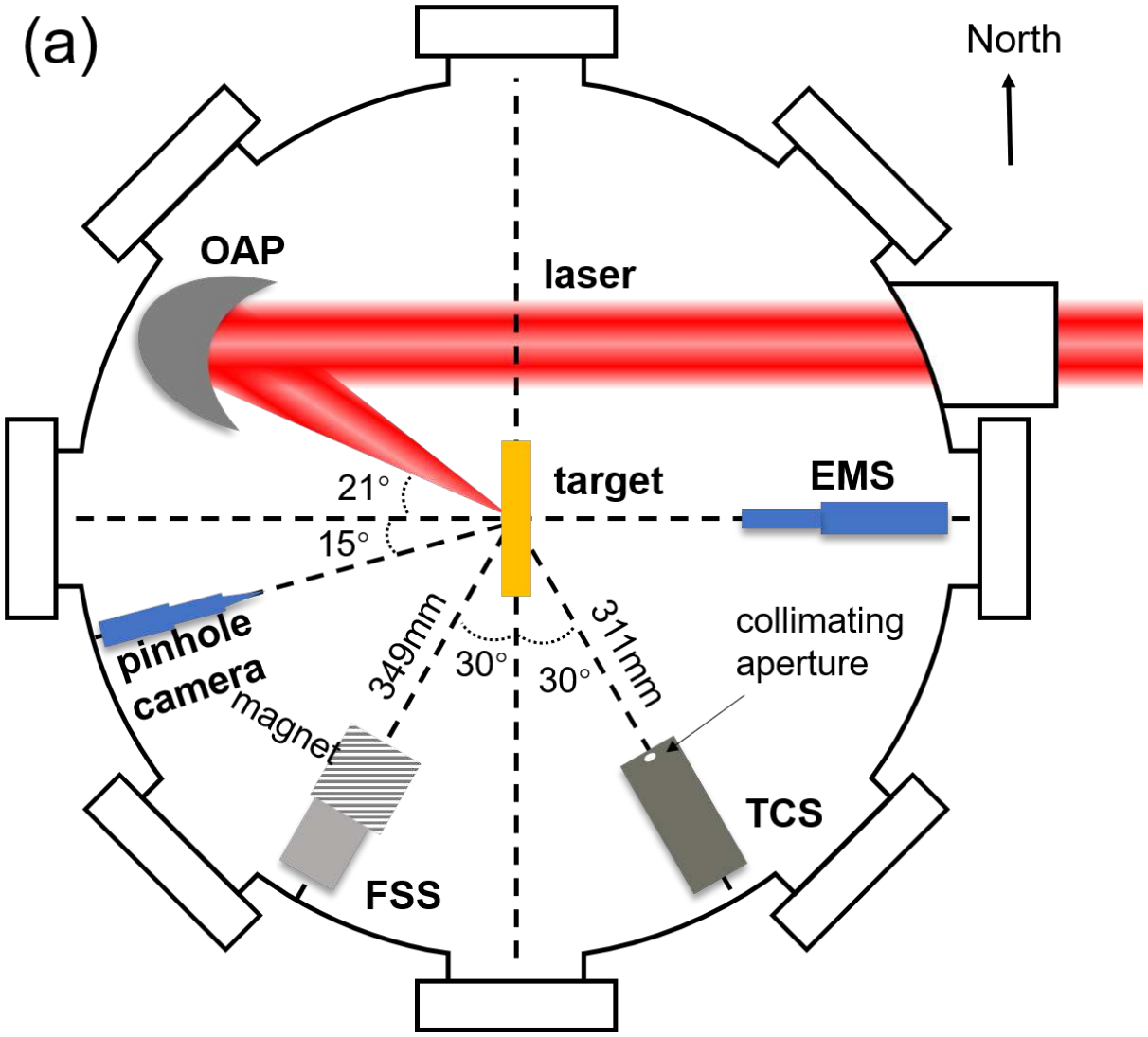

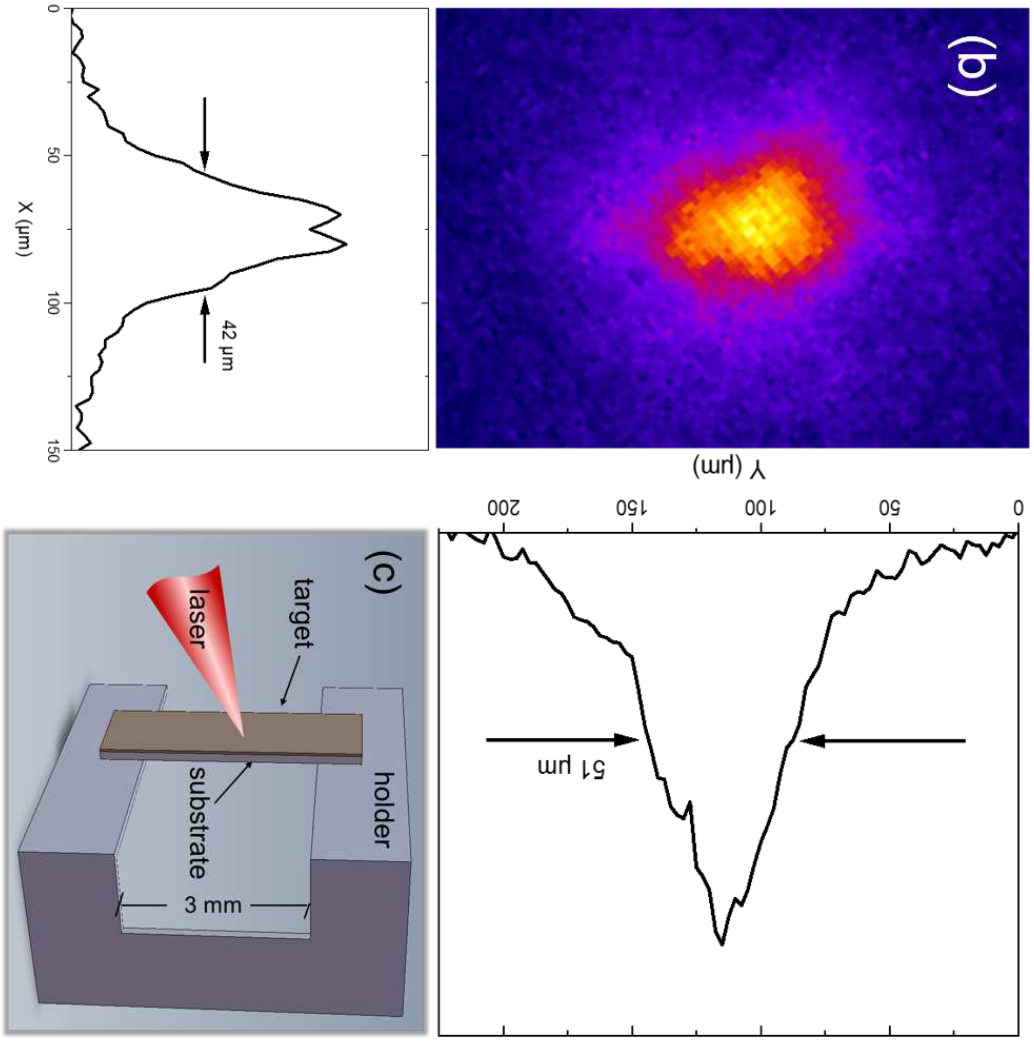

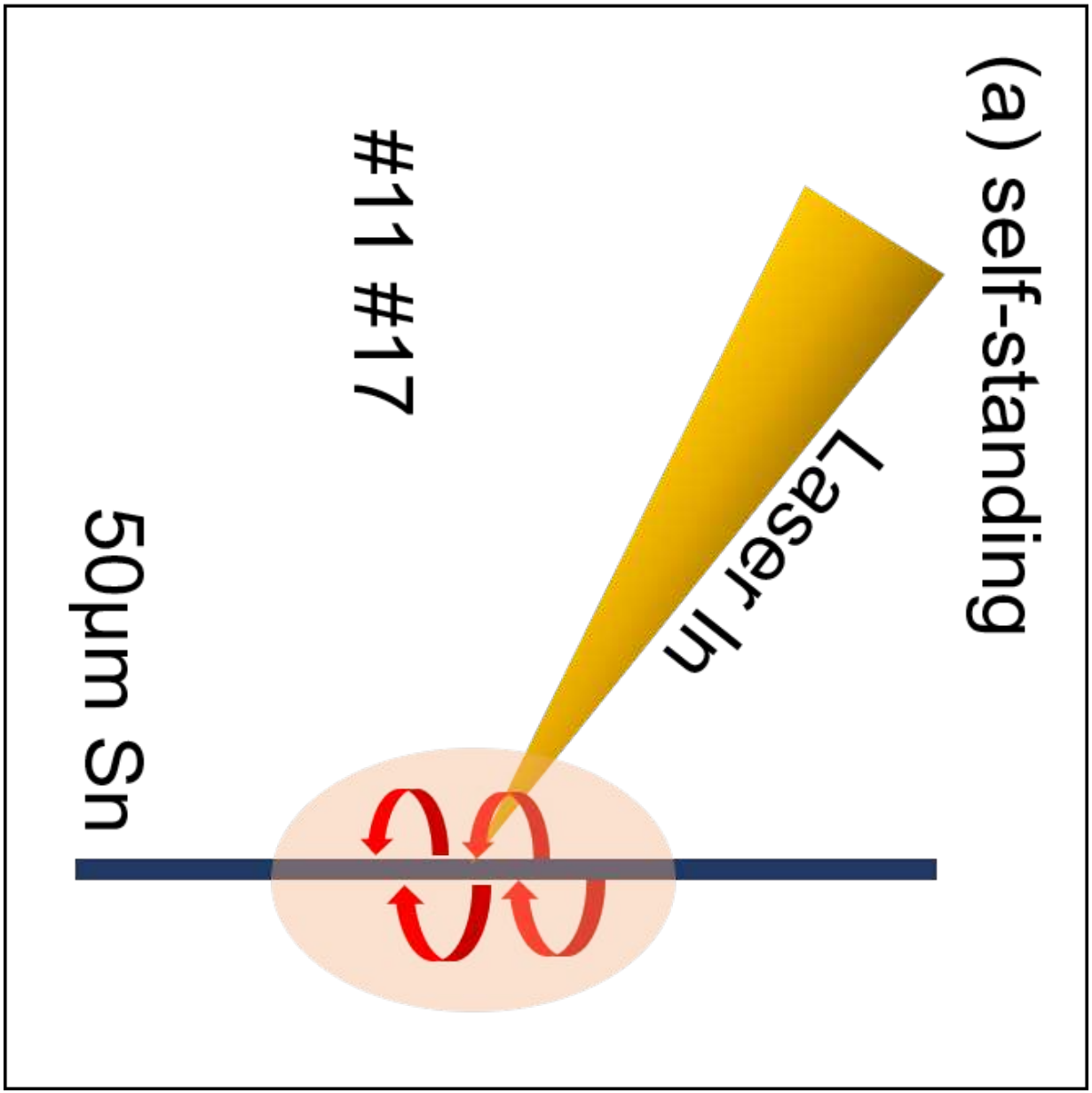

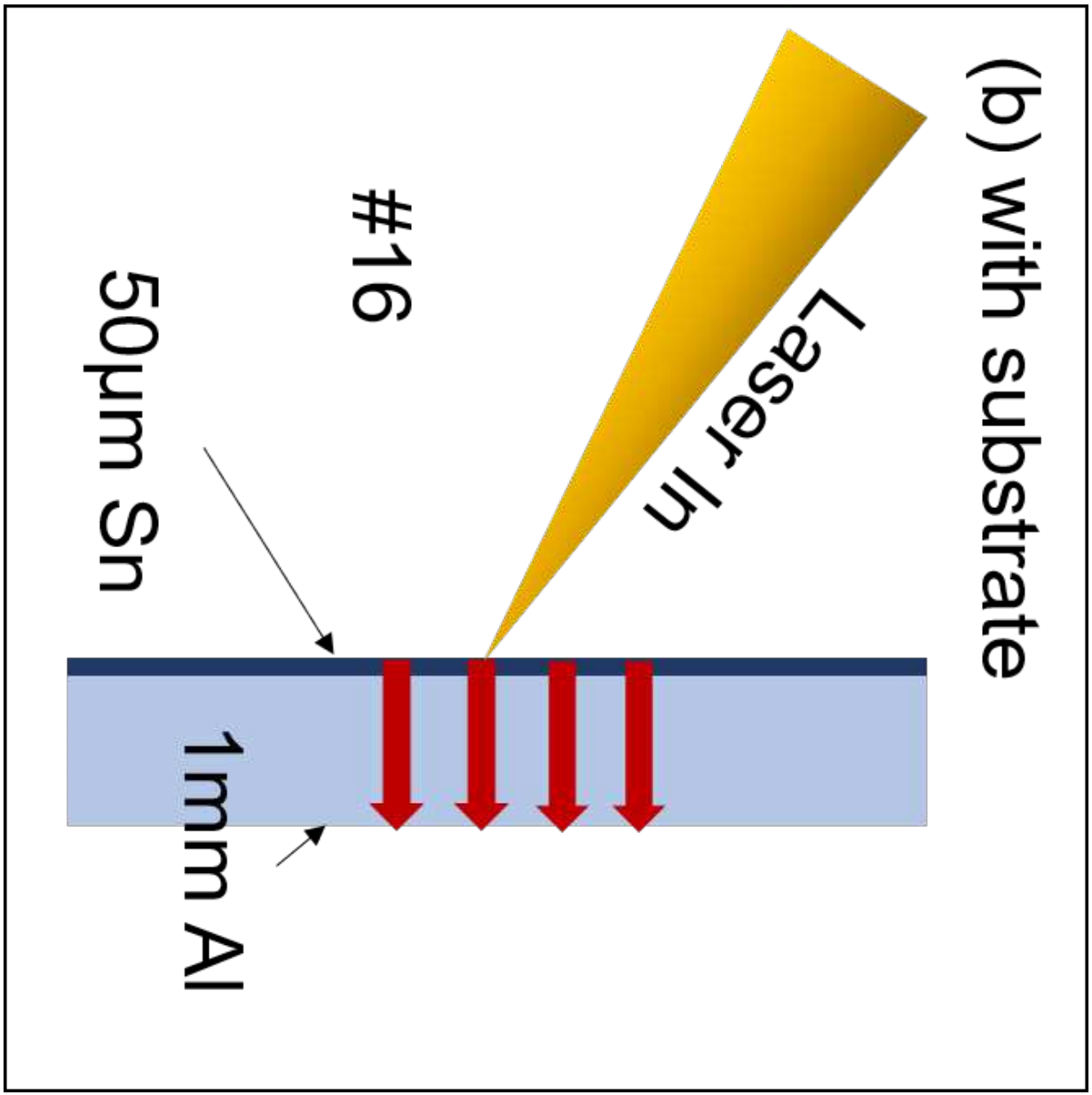

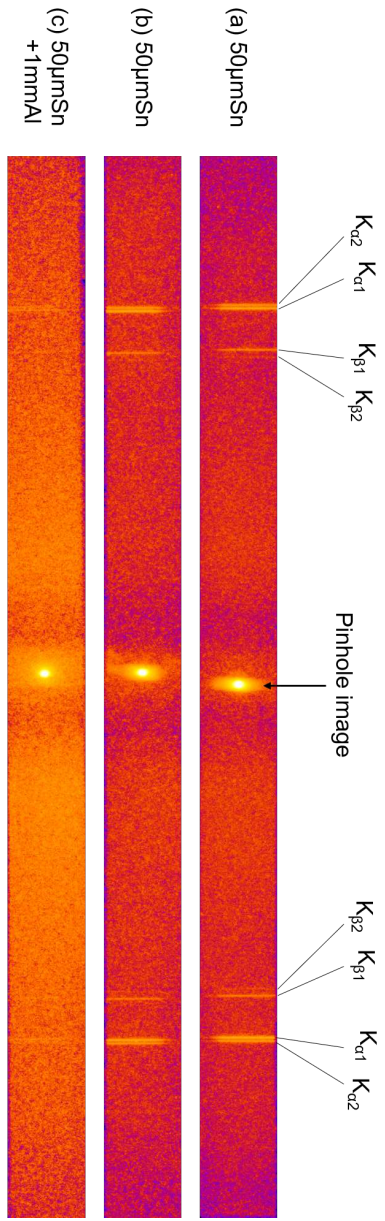

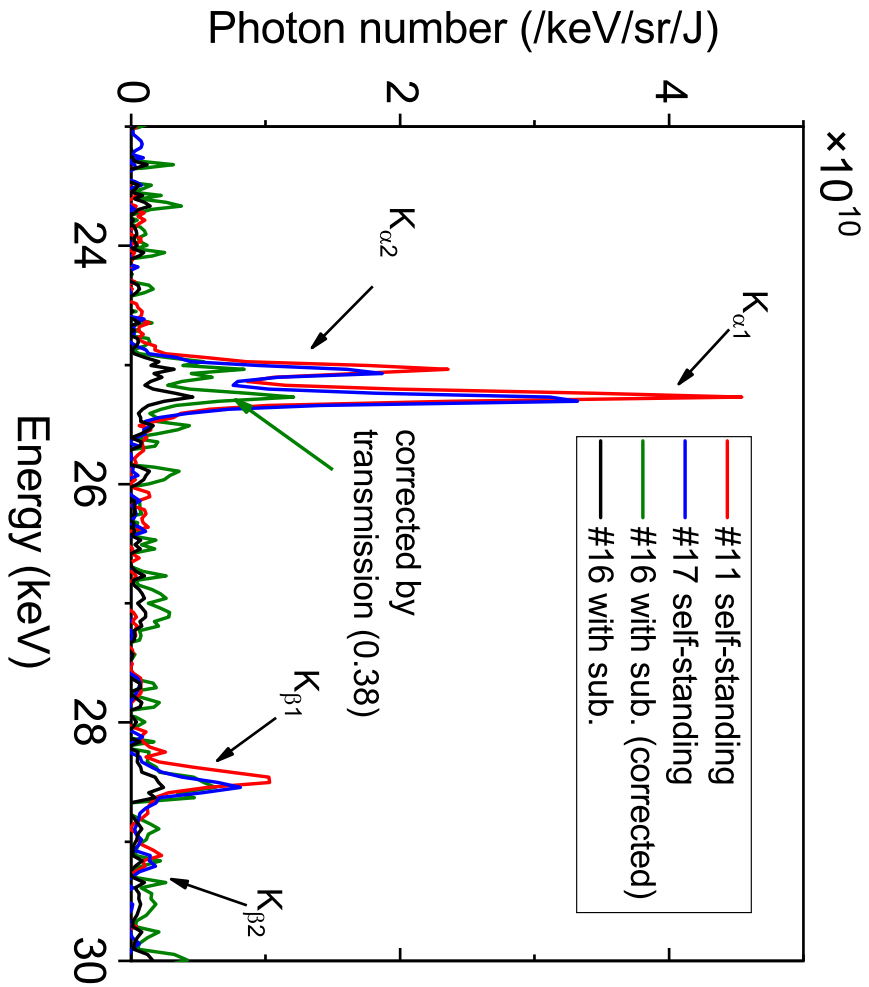

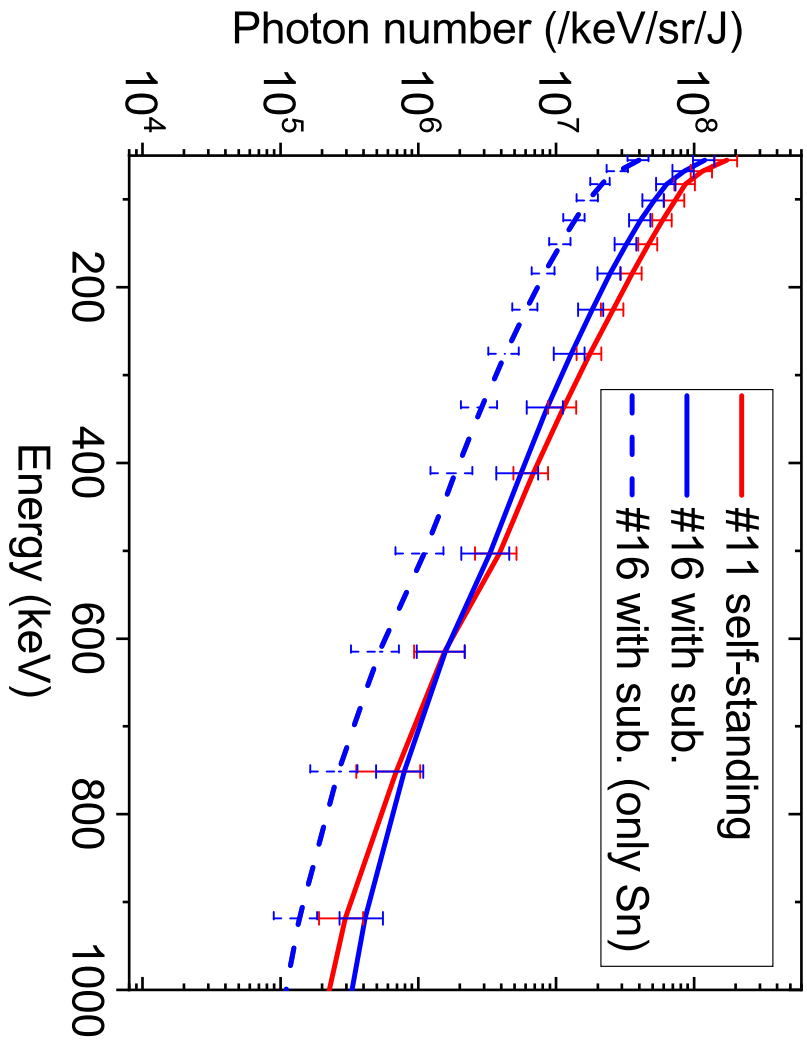

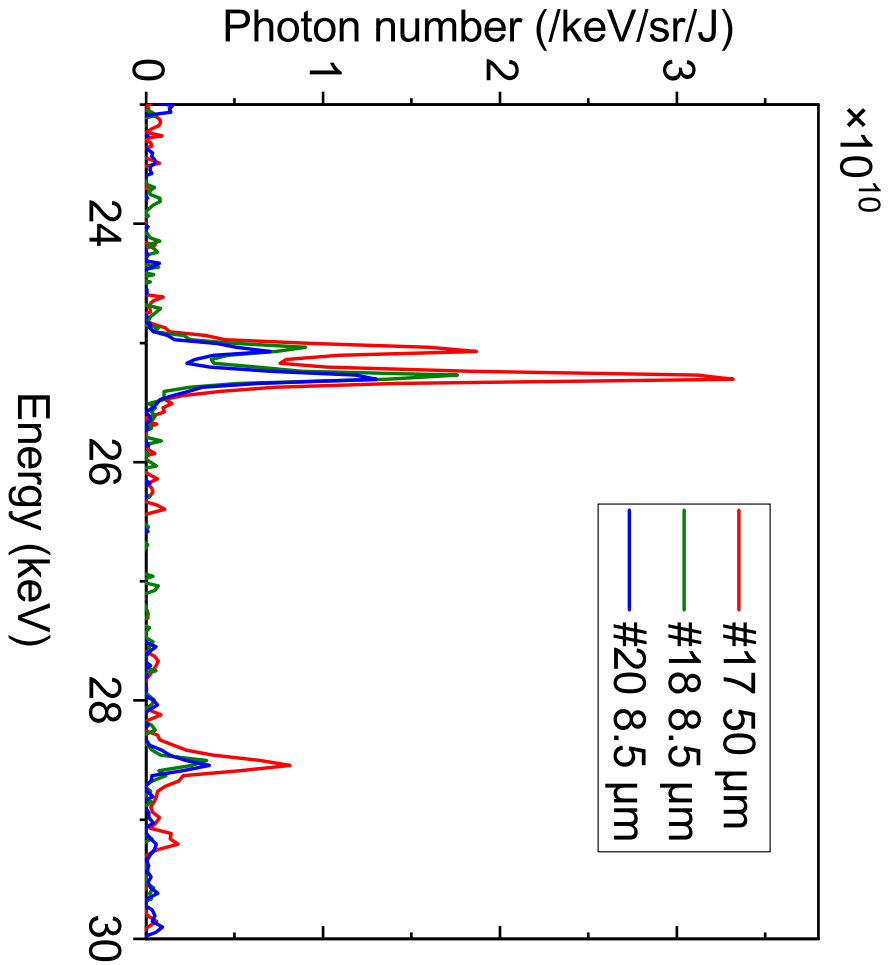

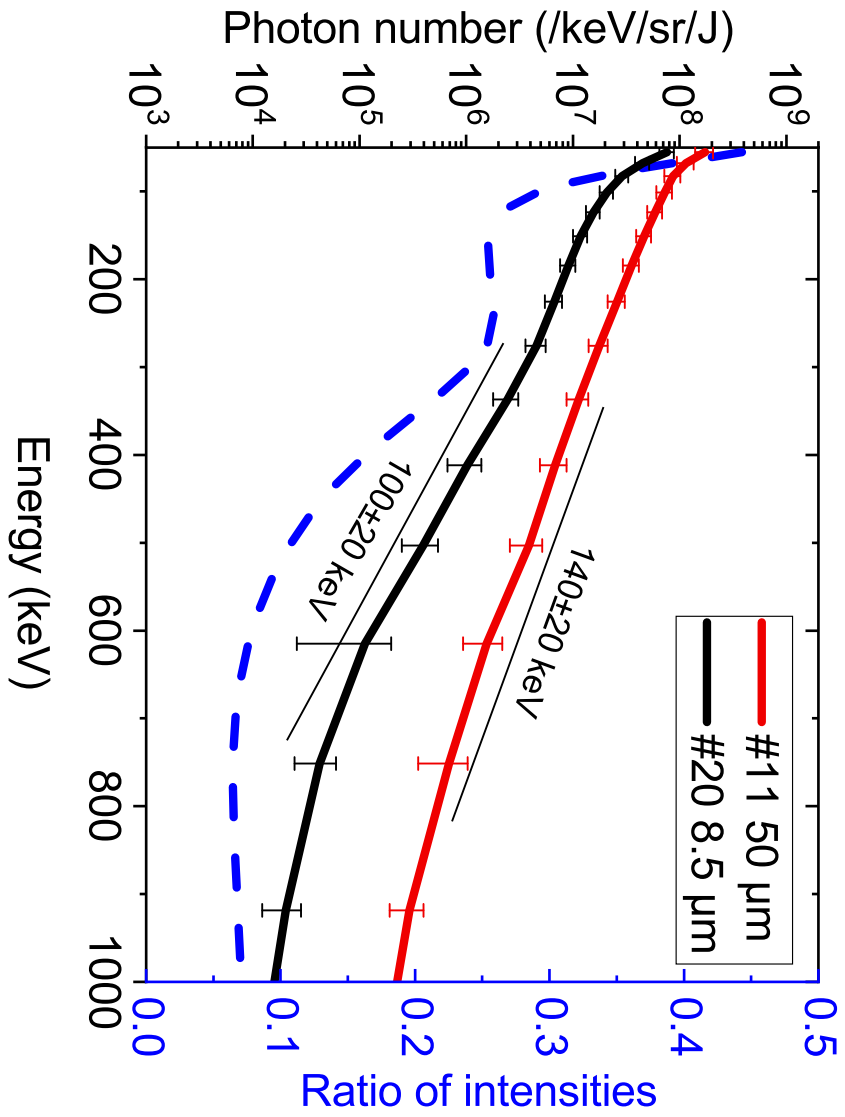

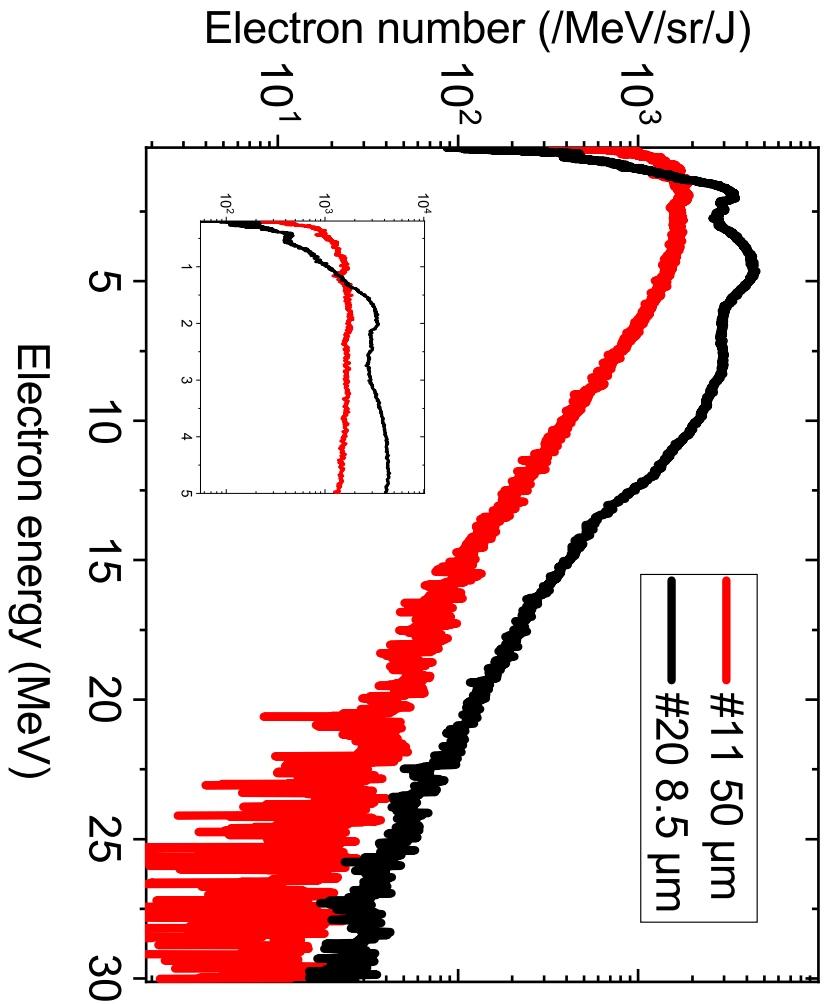

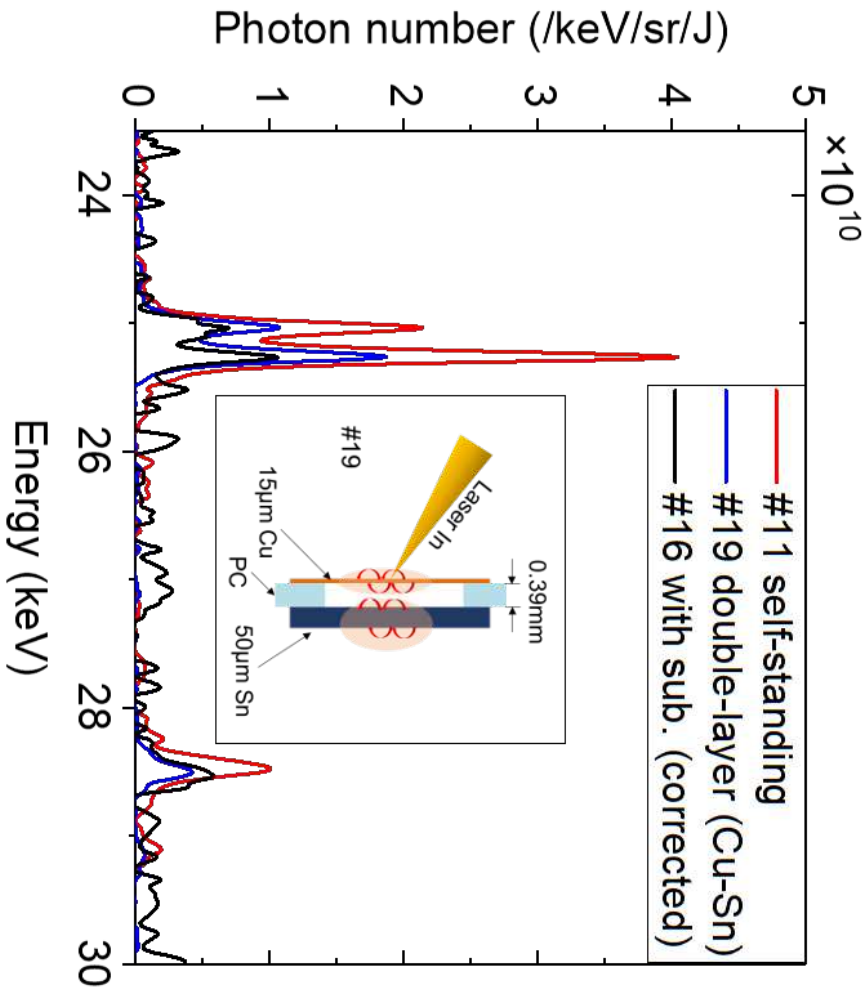

AIP Publishing

Physics of Plasmas

ACCEPTED MANUSCRIPT

PLEASE CITE THIS ARTICLE AS DOI: 10.1063/5.0064541